Journal of Materials Chemistry C



PAPER

View Article Online
View Journal | View Issue



Cite this: J. Mater. Chem. C, 2015, 3, 1567

Modification of the coordination environment of Eu²⁺ in Sr₂SiO₄:Eu²⁺ phosphors to achieve full color emission

Li-Cheng Ju,^a Xin Xu,^{*a} Lu-Yuan Hao,^a Yue Lin^b and Ming-Hsien Lee^c

Sr₂SiO₄:Eu²⁺ phosphors were synthesized by a conventional solid state reaction method. After a low amount of nitrogen (~1 mol% of oxygen) was incorporated to modify the local coordination environment of Eu²⁺, the phosphor showed a single intense broad band emission centered at 625 nm under blue light (453 nm) excitation, and three emission bands (480, 555 and 625 nm) under ultraviolet irradiation. The incorporation of nitrogen was confirmed by X-ray photoelectron spectroscopy (XPS), Fourier-transform infrared spectroscopy (FT-IR) and absorption spectroscopy. 480 and 555 nm emissions originated from Eu²⁺ ions occupying the Sr(I) sites and Sr(II) sites in the Sr₂SiO₄ crystal, respectively, while 625 nm emission originated from the nitrogen coordinated Eu²⁺ ions. The local coordination structure around Eu²⁺ ions in the red phosphors was analyzed with the aid of density functional theory based first principles calculations. The analysis showed that nitrogen should preferentially substitute the O5' sites around Eu2+ in Sr(III) sites, which agreed fairly well with the experimental results from the X-ray absorption fine structure (XAFS) and the electron paramagnetic resonance (EPR) spectra. The electronic structure analysis confirmed the lowered center of gravity of Eu 5d energy states and the broadened Eu 4f energy states, which are due to the tightened coordination environment and the hybridization of the 4f states of Eu and 2p states of nitrogen-oxygen, leading to a red emission. The novel nitrogen modified Sr₂SiO₄:Eu²⁺ could serve as a full color phosphor for near-UV LEDs or a red-emitting phosphor for blue LEDs.

Received 3rd July 2014 Accepted 6th December 2014

DOI: 10.1039/c4tc01435a

www.rsc.org/MaterialsC

1 Introduction

The InGaN-based white-light-emitting diodes (WLEDs) have attracted great attention due to their advantages in energy efficiency, long lifetime, compactness, environmental friendliness and designable features. As an indispensable constituent in WLEDs, the phosphors make big contributions to the color index and efficiency.

Among the various phosphors, red phosphors play a key role in improving the color rendering properties of WLEDs and are most urgently in need of improvement. Traditional powerful red emitting phosphors (*i.e.* Y_2O_3 :Eu³⁺) cannot be used in WLEDs due to their line excitation and emission.¹ The sulfide phosphors (*i.e.* $Sr_{1-x}Ca_xS$:Eu²⁺) with stronger emission intensities under blue light excitation suffer from low stability against humid, thermal and radiative environments.²

Recently, oxynitride phosphors, such as CaAlSiN₃:Eu^{2+ 3-5} and $M_2Si_5N_8$:Eu²⁺ (M = Ca, Sr, and Ba),⁶⁻¹² were found to be very promising red phosphors. However, they require severe synthesis conditions, such as elevated pressure and temperature and the use of air-sensitive starting powders.^{10,13,14} To overcome these problems, it is essential to develop novel red phosphors that can be easily prepared and can emit bright red light under the excitation of near UV-blue lights.

As a type of traditional phosphor, Eu2+ doped strontium orthosilicate (Sr₂SiO₄) phosphors have attracted intense interest due to their special structural features and potential applications in developing WLEDs. 15-17 Sr₂SiO₄ has two crystallographic phases: monoclinic (β- Sr_2SiO_4) and orthorhombic (α'- Sr_2SiO_4). The two phases can coexist because the phase transformation occurs through a short-range rearrangement of the coordination structure without breaking any bonds. 18-20 There are two cation sites of Sr^{2+} in both β - Sr_2SiO_4 and α' - Sr_2SiO_4 phases: Sr(I)is ten-coordinated and Sr(II) is nine-coordinated by oxygen atoms within a limited range.21 When Eu occupies Sr(1) site with a weak crystal field, the emission band is about 470-490 nm, while the Sr(II) site has a more compact environment and a stronger crystal field effect, leading to a longer emission wavelength of 540-570 nm.20 Bond lengths in Sr polyhedra are scattered over a wider range of values in β-Sr₂SiO₄ phase than in

^aCAS Key Laboratory of Materials for Energy Conversion, Department of Materials Science and Engineering, University of Science and Technology of China, Hefei, Anhui 230026, P. R. China. E-mail: xuxin@ustc.edu.cn; Fax: +86-551-63601592; Tel: +86-551-63600824

^bHefei National Laboratory for Physical Sciences at the Microscale, University of Science and Technology of China, Hefei, Anhui 230026, P. R. China

^cDepartment of Physics, Tamkang University, New Taipei City 25137, Taiwan

the α' -Sr₂SiO₄ phases,²² leading to a slight blue-shift of Eu²⁺ in the β -Sr₂SiO₄ phase for both Sr(i) and Sr(ii) sites. Through structural modification, the Sr₂SiO₄:Eu²⁺ phosphors could be controlled to emit different colors in a wide range, from blue to vellow.²³

Recently, red-emitting Sr_2SiO_4 : Eu^{2+} phosphors have been reported through the incorporation of nitrogen. $^{24-26}$ Sr_2SiN_z - $O_{4-1.5z}$: Eu^{2+} (0.7 < z < 1.2) reported by Wang $et\ al.$ had a stoichiometric composition, 26 and the red emission was attributed to the overlap of the two bands due to the Eu(I) and Eu(II) sites, whereas $Sr_2Si(O_{1-x}N_x)_4$: Eu^{2+} reported by Kim $et\ al.$ was considered as a non-stoichiometric solid-solution with the substitution of N^{3-} for O^{2-} , 24,25 and the red emission was assigned to the Eu(II) sites. Both the studies focused on the photoluminescence properties and simply ascribed the red emission to the strong crystal field splitting and the nephelauxetic effect of N^{3-} . However, no detailed study has been done on the coordination environment of Eu^{2+} , and the interaction mechanism of nitrogen on red-shift emission.

Unlike previous studies, $^{24-26}$ where a large amount of nitrogen was incorporated, we succeeded in achieving a strong red-emission in $\rm Sr_2SiO_4:Eu^{2+}$ phosphors through the incorporation of a very small amount of nitrogen in this investigation. The preferential nitrogen substitution sites in the host lattice, the local structural deformation after nitrogen doping and the relationship between photoluminescence and the coordination environment of $\rm Eu^{2+}$ were determined with the aid of geometry optimization and electronic structure calculations, performed with the Cambridge Serial Total Energy Package (CASTEP) code. This code employs density functional theory (DFT), pseudopotential, and a plane-wave basis set to provide a good atomic-level description of all types of materials and molecules.

2 Experimental section

2.1 Synthesis

Nitrogen modified $Sr_2SiO_4:Eu^{2+}$ phosphors (denoted as NSSO) were prepared by a traditional solid-state reaction method. A mixture of $1.97SrCO_3-0.97SiO_2-0.01Si_3N_4-0.015Eu_2O_3$, as the raw materials, was calcined at $1500\,^{\circ}C$ for 4 h in BN crucibles by a tube furnace under flowing NH $_3$ atmosphere. Both the heating and cooling rates were $300\,^{\circ}C$ h $^{-1}$. For comparison, $Sr_2SiO_4:Eu^{2+}$ phosphors (denoted as SSO) were synthesized by firing a mixture of $1.97SrCO_3-SiO_2-0.015Eu_2O_3$ under the same preparation procedure. The produced samples were benignly crushed into fine powders. We used $Sr_2Si_5N_8:Eu^{2+}$ phosphor as the reference for red light emission, which was prepared by a solid-state reaction method in our laboratory.

2.2 Characterization

The crystalline phases developed in the final products were identified by X-ray diffraction analysis (XRD, Philips PW 1700; Cu $K_{\alpha 1}$ radiation; scanning rate of 2° min $^{-1}$), adding KCl as the internal standard. The ratio of $\alpha'\text{-Sr}_2\text{SiO}_4$ phase to $\beta\text{-Sr}_2\text{SiO}_4$ phase was calculated based on the intensity of distinguishable peaks around 27.5° .

The photoluminescence (PL) spectra under UV-vis excitation were measured using a fluorescent spectrophotometer (F-4600, Hitachi Ltd., Japan) with a 200 W Xe lamp as the excitation source. High temperature luminescence measurements were carried out on the same spectrophotometer equipped with a heating element. The absorption spectra were recorded with a UV-vis-NIR spectrophotometer equipped with an integrating sphere (SolidSpec-3700, Shimadzu, Tokyo, Japan).

The quantum efficiencies (QE) were determined with a 200 W Xe lamp as an excitation source and a Hamamatsu MPCD-7000 multichannel photodetector. The decay curves were measured by a steady state/transient fluorescence spectrometer (JY Fluorolog-3-Tou, Jobin Yvon, France).

The morphology of the synthesized phosphors was observed by scanning electron microscopy (SEM, JED-2300, JEOL, Japan). High resolution transmission electron microscopy (HRTEM) images and diffraction patterns were obtained from a spherical aberration corrected JEM-ARM 200F.

X-ray photoelectron spectroscopy (XPS) measurements were performed on an ESCALAB 250 high performance electron spectrometer using a monochromatized Al $K\alpha$ excitation source.

Fourier-transform infrared spectra (FT-IR) were measured on a Nicolet 8700 spectrophotometer in the range of 400–4000 cm $^{-1}$ using the KBr pellet (\sim 1 wt%) method. Each analysis consisted of a minimum of 32 scans and the resolution was 4 cm $^{-1}$.

The X-ray absorption spectra at Eu $\rm L_3$ -edge were measured on the beam line BL14W1 of Shanghai Synchrotron Radiation Facility (SSRF) in Shanghai, China. The electron beam energy was 3.5 GeV and the mean stored current was 300 mA.

Room temperature electron paramagnetic resonance (EPR) spectra were obtained using a JEOL JES-FA200 EPR spectrometer (300 K, 9.057 GHz, X-band). Microwave power employed was 1 mW; sweep width ranged from 2800 to 3700 G. Modulation frequency and modulation amplitude were 100 kHz and 3.5 G, respectively.

2.3 First principles calculation

We calculated the crystal structures' optimization and electronic structures of the SSO and NSSO phosphors by first principles method. Based on the experimental data, we used Eu doped α' -Sr₂SiO₄ (SSO) as the control group. We built a 1 \times 2 \times 1 supercell of α' -Sr₂SiO₄ and replaced one Sr with Eu in the cell as the SSO model. Then, we substituted all the oxygen atoms that were coordinating with Eu by nitrogen to establish one NSSO model. These models were optimized using the Cambridge Sequential Total Energy Package (CASTEP) computational codes. These calculations employ the density functional theory plane-wave pseudopotential method. The PBE method by Generalized Gradient-corrected Approximation (GGA) was used for the exchange correlation potential. The optimized lattice structures were used for calculating the electronic structures and density of states of these phosphors. The basic parameters for both parts were chosen as follows: the kinetic energy cut-off was 430 eV, sets of k points were $4 \times 2 \times 3$, self-consistent field tolerance thresholds were 1.0×10^{-6} eV per atom and the space representation was reciprocal. The reliability of the calculation

15 40 SEI

was demonstrated by the result of the convergence test. We used a 1.9 eV scissors operator to plot the band structure of SSO to compare it with NSSO.

3 Results and discussion

Phases and photoluminescence properties

Fig. 1 shows the XRD patterns of SSO and NSSO phosphors. All the diffraction peaks could be attributed to Sr₂SiO₄ phases. SSO only shows the monoclinic (β-Sr₂SiO₄) phase, which is in good agreement with that reported before.20 NSSO exhibits mainly the orthorhombic phase (α' -Sr₂SiO₄) with about 30% β -Sr₂SiO₄.

Fig. 2 shows electron microscope images of SSO and NSSO phosphors. The mostly equiaxed shaped crystals of 5-10 µm size can be seen for both the phosphors. The nitrogen incorporation exhibits little influence on the morphology and particle size of the phosphors.

Fig. 3 shows the photoluminescence properties of SSO, NSSO and Sr₂Si₅N₈:Eu²⁺ phosphors. SSO exhibits two emission bands centered at 470 nm from Eu ions in Sr(1) sites and 540 nm from Eu ions in Sr(II) sites, which is in good agreement with the values reported previously.20,31 However, the NSSO phosphor shows an extra emission peak at 625 nm besides the two traditional peaks at 480 nm and 555 nm. As reported previously,20 the pure α'-Sr₂SiO₄:Eu²⁺ phosphor exhibits two emission bands centered at 490/570 nm. Because NSSO contains a small amount of β phase, we can conclude that the 480 nm emissions of the NSSO phosphors are from Eu ions in Sr(1) sites of α' and β phases, and the 555 nm emissions are from Eu ions in Sr(II) sites of α' and β phases, as reported before.²⁰ In addition, the emission band centered at 625 nm is very similar to the emission spectra of Sr₂Si₅N₈:Eu²⁺ phosphor.¹³ Considering the similar shapes of their excitation spectra, we can infer that some of the Eu2+ ions in the NSSO phosphor are coordinated with nitrogen. Photoluminescence properties indicate that the NSSO phosphors could serve as full color phosphors for near-UV LEDs or red-emitting phosphors for blue LEDs. Fig. 4 shows the SSO and NSSO phosphors under 365 nm excitation and under

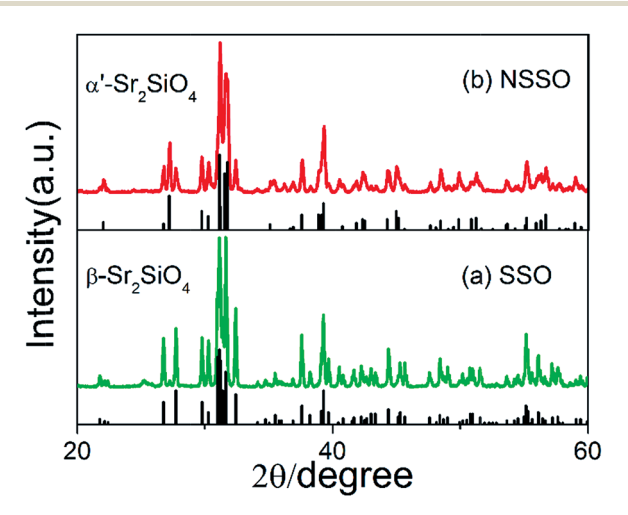


Fig. 1 The XRD patterns of (a) SSO and (b) NSSO.

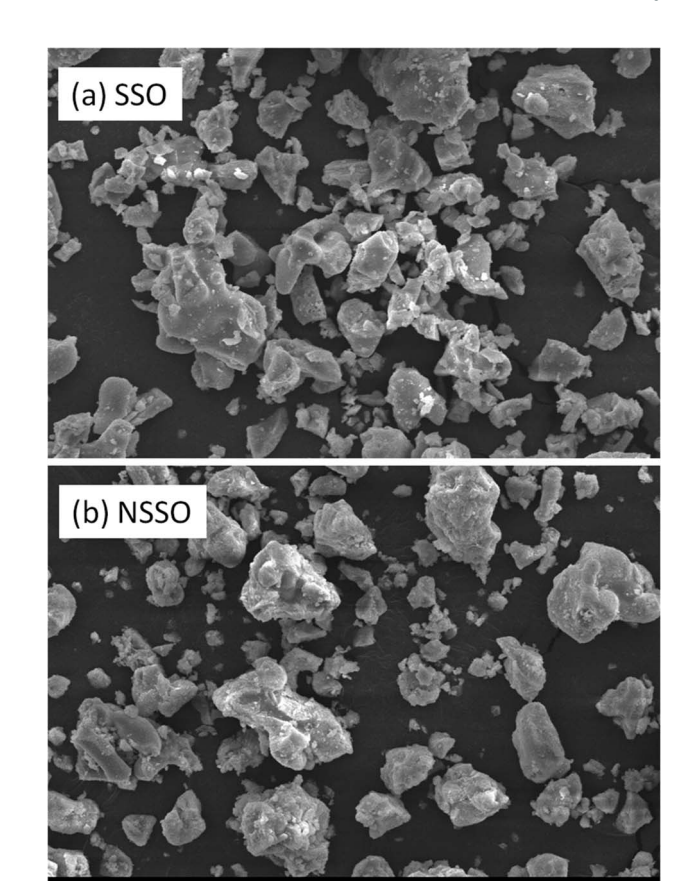


Fig. 2 SEM image of (a) SSO and (b) NSSO phosphors.

X1.000

natural light. The SSO phosphor appears considerably different from the NSSO phosphor, which is in good agreement with their photoluminescence properties.

The decay for the 625 nm emission of NSSO under 453 nm excitation could be fitted using one exponential function with a decay time of 1037 ns, which is similar to 1360 ns of Sr₂Si₅-N₈:Eu²⁺.32 The external QE of the red emission of NSSO at the excitation wavelength of 453 nm reaches 68.4%, which is expected to be increased through removing the small particles shown in Fig. 2.

Fig. 5 plots the corresponding Commission Internationale de l'Eclairage (CIE) 1931 chromaticity coordinates. The CIE color coordinates of NSSO indicates its high color saturation; thus, it could compensate for the red color deficiency of the current cold YAG:Ce³⁺-based WLEDs.³³ A white-emitting LED lamp presenting a warm color temperature of 4814 K has been realized using the NSSO phosphor in combination with the commercial YAG:Ce3+ phosphor, as shown in the lower right inset of Fig. 5. The CIE chromaticity coordinates (0.345, 0.307) for the fabricated LED lamp lie in the white light region. The emission spectrum of the LED lamp is also shown in the upper right inset of Fig. 5, which exhibits a good color rendering index of 91 for R_a . The CIE chromaticity coordinates (x, y) and the correlated color temperature (CCT) for the fabricated LEDs can be tuned by changing the addition amount of NSSO.

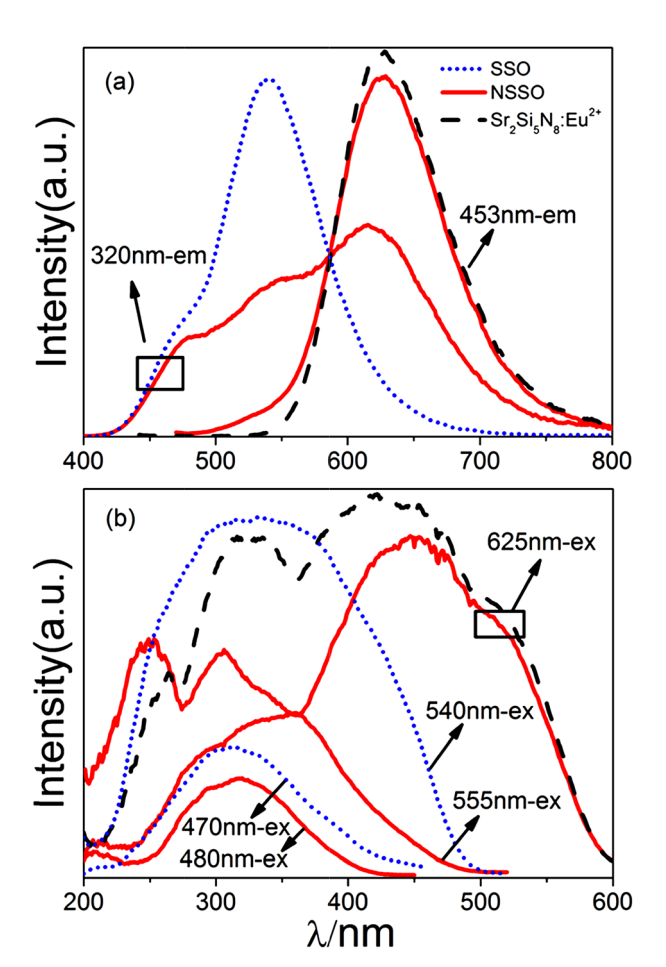


Fig. 3 The (a) emission and (b) excitation spectra of SSO (\cdots) , NSSO (\cdots) and Sr₂Si₅N₈:Eu²⁺ phosphor (---).



Fig. 4 Images of SSO and NSSO under UV and natural light.

The thermal stability of phosphors plays a key role in the high power WLEDs. Fig. 6 shows the temperature dependence of the PL properties for the SSO and NSSO phosphors under the

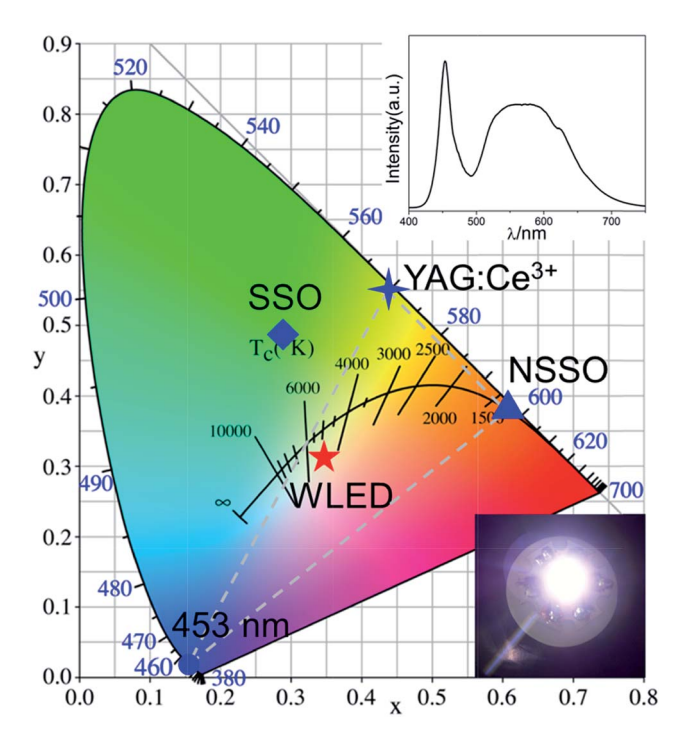


Fig. 5 The CIE color coordinates of SSO (excited by 320 nm), NSSO (excited by 453 nm), commercial YAG:Ce³⁺ (excited by 453 nm) and a white-emitting GaN-based LED packaged by NSSO and commercial YAG:Ce³⁺ phosphor (insets: emission spectra of the wLED [upper right] and the real image of it [lower right]).

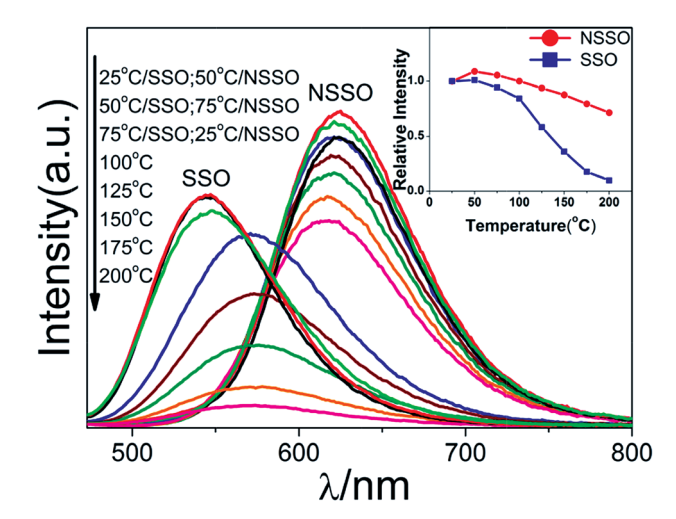


Fig. 6 Temperature dependence of emission spectra of SSO and NSSO excited at 453 nm. The inset shows the variation of PL intensity as a function of temperature.

excitation at 453 nm. The inset shows the variation of PL intensity as a function of temperature. SSO exhibits a steady loss of emission intensity with the increase in temperature and retains only about 36.0% of the initial intensity when the measuring temperature is up to 150 °C. For NSSO, PL intensity initially increases with the temperature. With the increase in the temperature up to 150 °C, NSSO only shows a decrease of 12.3%. It should be pointed out that the pure α' Sr₂SiO₄:Eu²⁺

phosphor²⁰ exhibits similar thermal quenching properties (intensity remains about 41% at 150 °C) as SSO, indicating that the thermal stability of NSSO could not be attributed to the α' phase. High temperature will increase the probability of nonradiative transition, which is caused by the thermal activation and release of the luminescent center through the crossing point between the excited state and the ground state. The activation energy of non-radiative transition increases with the increase of the crystal stiffness and the decrease of the Eu²⁺ mobility. The nitrogen coordination will suppress the Eu²⁺ vibration, which could also be confirmed by the smaller Stokes shift (\sim 6000 cm⁻¹) of NSSO, compared with that (\sim 10 000 cm⁻¹) of SSO.

The blue-shift of NSSO with increasing temperature could be explained by the thermally active phonon-assisted tunnelling from the excited states of the lower-energy emission band to those of the higher-energy emission band in the configuration coordinate diagram. 24,28 The red-shift of SSO with increasing temperature could be attributed to the Varshni equation, 35 which points out that the increase in temperature reduces the transition energy between the excited and ground states. However, the sudden red-shift of the emission wavelength in SSO is due to the phase transformation from β - to α' -Sr $_2$ SiO $_4$ at 85 $^{\circ}$ C because the phase transformation occurs through a shortrange rearrangement of the coordination structure without breaking any bonds. 21,36

As previously reported, a complex phosphor consisting of 64 wt% $Sr_2Si_5N_8$: Eu^{2+} and 36 wt% Sr_2SiO_4 : Eu^{2+} was obtained through the chemical reaction of $SrCO_3$, Eu_2O_3 , and Si_3N_4 .³⁷ However, this phosphor strangely exhibited equivalent optical properties to pure $Sr_2Si_5N_8$: Eu^{2+} phosphors. Based on our research, the Sr_2SiO_4 : Eu^{2+} obtained there actually is the nitrogen modified Sr_2SiO_4 : Eu^{2+} , which has comparable photoluminescence with $Sr_2Si_5N_8$: Eu^{2+} phosphors.

3.2 Experimental results related to structural and photoluminescence features

Fig. 7 shows the selected area electron diffraction (SAED) pattern and corresponding lattice image of the NSSO phosphor. The SAED pattern of NSSO phosphor is successfully indexed with the orthorhombic α' -Sr₂SiO₄ cell and clearly shows the existence of long periodicity. The corresponding lattice image confirms that the crystal is characterized by a superlattice structure. However, the periodicity is not regular throughout the whole lattice area, as shown in Fig. 7. Some long periodicities include six interplanar spacings of (200), which is a systematic absent crystal plane in the normal lattice and appears under the effects of the modulated structure. Moreover, eight interplanar spacings' long periodicity is also presented in our lattice image. The formation of a superlattice is due to the ordered doping of impurity atoms. Based on our experimental data, the SSO phosphor does not show a superlattice structure (not shown here). Therefore, we exclude the possibility of the ordered doping of Eu ions and conclude that it is the ordered doping of nitrogen that leads to the superlattice structure of NSSO. Then, a slight non-regular long periodicity indicates that

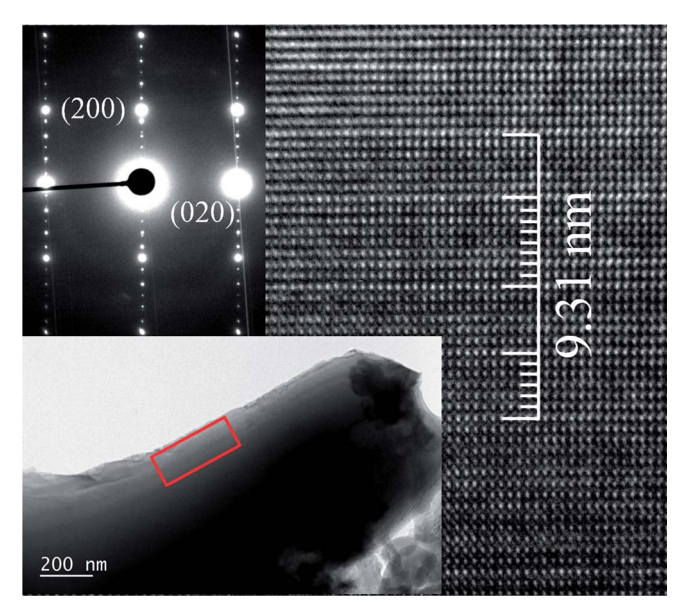


Fig. 7 Selected area electron diffraction pattern and corresponding lattice image of NSSO phosphor. Incident beam is almost parallel to the orthorhombic c-axis.

the nitrogen impurity does not show a perfectly ordered distribution in the base material. From Fig. 7, we can calculate that the average long periodicity is about 2.325 nm, which is about six and a half interplanar spacings of (200).

Fig. 8 shows the XPS spectra of SSO and NSSO. NSSO has nitrogen impurity appearing in their surfaces, which provides chemical foundations for the formation of microstructures similar to nitride. In contrast, SSO phosphor does not show peaks of N 1s electrons.

Fig. 9 exhibits the FT-IR spectra of SSO, NSSO and Sr_2Si_5 - N_8 : Eu^{2+} phosphors. The peak of Sr/Eu-N bond vibration

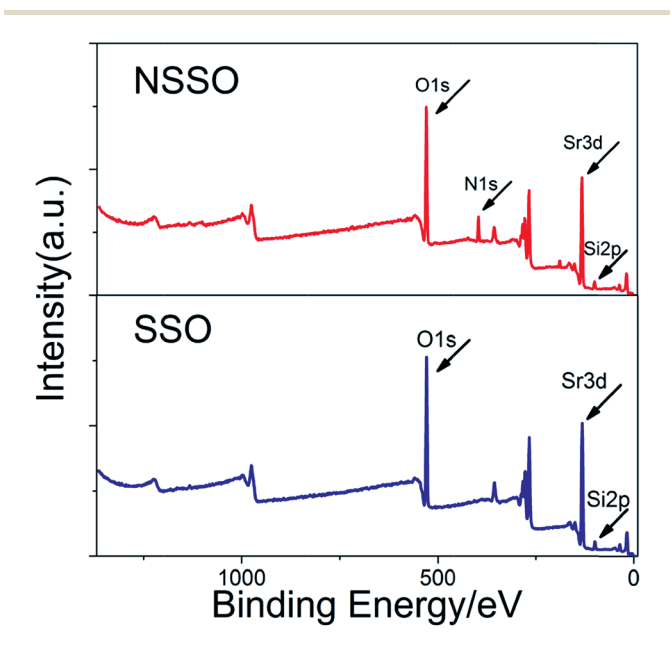


Fig. 8 XPS spectra of SSO and NSSO phosphors.

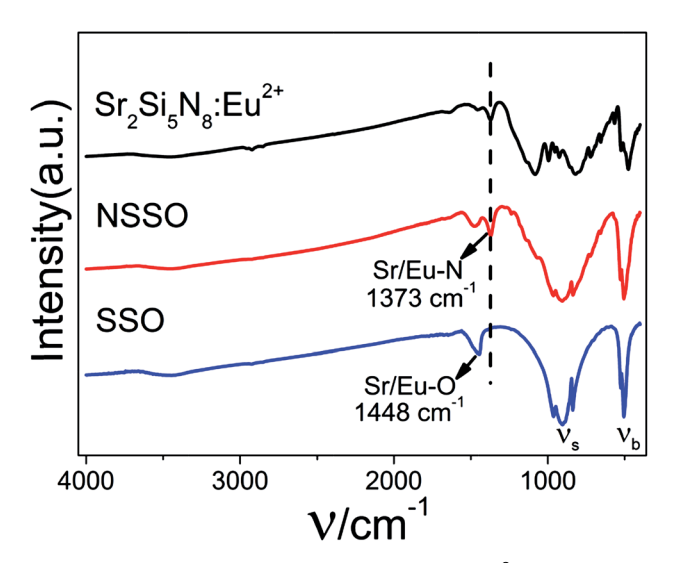


Fig. 9 FT-IR spectra of SSO, NSSO and Sr₂Si₅N₈:Eu²⁺ phosphors.

appears in NSSO, while the SSO sample does not show such peaks. The Absorption spectra relate to the PL properties because most of the absorbed energy can turn into the excitation energy. Fig. 10 shows the absorption spectra of the SSO, NSSO and $\rm Sr_2Si_5N_8:Eu^{2+}$ phosphors. The absorption spectrum of NSSO at shorter wavelength is similar to that of the $\rm Sr_2Si_5N_8:Eu^{2+}$ phosphor. It appears that the absorption spectrum of NSSO is a combination of SSO and $\rm Sr_2Si_5N_8:Eu^{2+}$ phosphors. Fig. 9 and 10 confirm that nitrogen does enter the crystal structure and forms chemical bonds with surrounding Sr/Eu ions in the NSSO phosphor.

Based on the above experimental results and their XRD patterns in Fig. 1, we conclude that $Sr_2SiO_4:Eu^{2+}$ phosphor can tolerate a local structural modification around Eu^{2+} ions through nitrogen incorporation. This might be partly attributed to the chemical similarity of oxygen and nitrogen. Another important reason is the slack lattice structure and loosely coordinated metal ions in the Sr_2SiO_4 crystal structure; in other

Fig. 10 Absorption spectra of SSO, NSSO and $Sr_2Si_5N_8$: Eu^{2+} phosphors.

words, the high freedom of motion of components or rotation in the crystals. Actually, the nitrogen content in the $\rm Sr_2SiO_4:Eu^{2+}$ phosphor could also be varied in a large range, but all the variations show similar photoluminescence properties, which is in good agreement with that reported before. ²⁶ In our opinion, only the nitrogen that is directly coordinated to $\rm Eu^{2+}$ could modify the photoluminescence properties. Incorporation of a large amount of nitrogen might lead to its entry in the host crystal, which may have little influence on the photoluminescence properties.

To obtain direct information about the local coordination environment surrounding the Eu^{2+} ions, Fig. 11 shows the Fourier transformed Eu L_3 -edge extended X-ray absorption fine structure (EXAFS) spectra of SSO, NSSO and $Sr_2Si_5N_8$: Eu^{2+} phosphors.

A precise investigation of the O and N atoms coordinated with $\mathrm{Eu^{2^+}}$ could not be achieved from EXAFS due to the complexity of the crystal structure and the lack of a model compound. However, a qualitative description could be given based on the EXAFS results. The average coordination distance of the first layer surrounding the $\mathrm{Eu^{2^+}}$ ions in the $\mathrm{Sr_2Si_5N_8:Eu^{2^+}}$ phosphor is much shorter than that in SSO phosphor, which could be ascribed to the short Eu–N bonding length. By comparing the EXAFS spectra of SSO and NSSO, we can clearly see that the first coordination shell around $\mathrm{Eu^{2^+}}$ ions in NSSO has much shorter coordination distance.

EPR is a powerful tool for studying the coordination environment of Eu²⁺ ions. Fig. 12 gives the electron paramagnetic resonance (EPR) results of SSO and NSSO. The resonant peaks are very complicated and difficult to be theoretically treated due to two reasons: (1) the spin-orbital coupling effect for the unpaired electrons in 4f orbitals; (2) Eu²⁺ ions are coordinated within the crystal field.³⁹ However, obvious differences can be observed in the results. The EPR peak width of NSSO is broader than that of SSO. We attribute this to the lifetime broadening, which results from the spin-lattice interaction.³⁹ Based on the

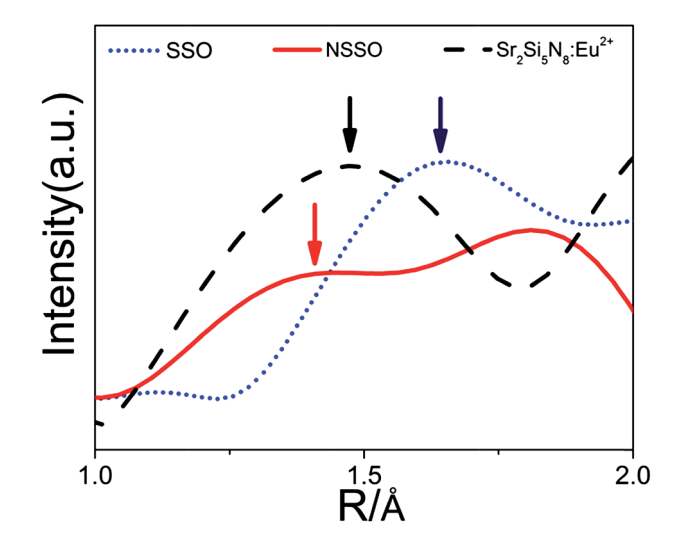


Fig. 11 Fourier transformed EXAFS spectra of SSO (…), NSSO (—) and $Sr_2Si_5N_8{:}Eu^{2+}$ phosphors (– – –).

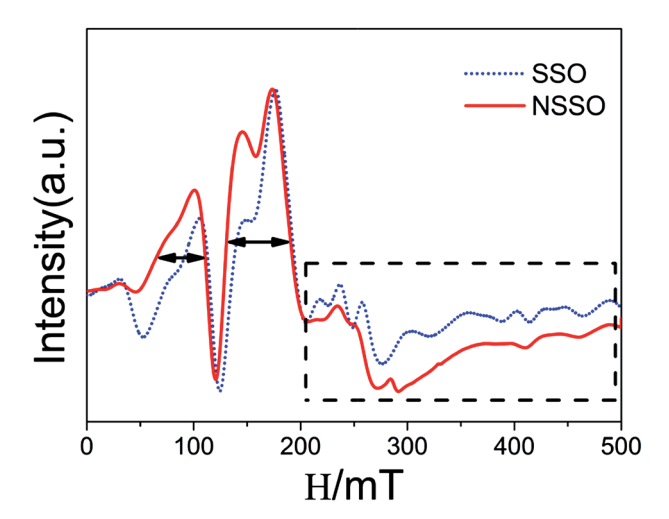


Fig. 12 EPR spectra of SSO and NSSO.

uncertainty principle, the stronger the interaction, the smaller is the electrons' lifetime deviation, the bigger is the bias of the magnetic field intensity, and therefore the broader the peak width is. Thus, it is clear that the unpaired electrons of Eu²⁺ ions in NSSO interact more intensively with the coordinated lattice and the crystal field around them is stronger.

3.3 First principles calculation

The experimental results in the previous sections show that the incorporation of a small amount of N in the lattice of Sr_2 - SiO_4 : Eu^{2+} leads to a new red emission. It is important to explore the mechanism of the red emission through first-principles calculations. 29,30,40

As can be seen in Fig. 13, there are six types of oxygen in either Sr(I) or Sr(II) site according to their coordination distance and crystal symmetry. Two SSO models could be built with one of the two Sr sites occupied by Eu. Because of the small amount

of nitrogen incorporation, it is reasonable to assume that only one oxygen is replaced by N in the supercell. Thus, we substituted each type of oxygen surrounding Eu by a nitrogen to establish the NSSO models.

We first carried out full geometry relaxation for all the NSSO models. Fig. 14 summarizes the total energies calculated for the different relaxed configurations. The model in which Eu occupies the $Sr(\pi)$ site and nitrogen occupies the OS' site has the lowest energy, indicating that this is the most stable configuration for NSSO and will be used for further calculations.

The bond length distributions of Eu–O in two SSO models and Eu–N in twelve NSSO models are shown in Fig. 15. Almost all the bond lengths become shortened after the oxygen is replaced by nitrogen. For example, an obvious shortening appears in the Eu2N5′ model, which is the most stable configuration for NSSO. Based on these results, we can ascribe the shorter coordination distance, shown in Fig. 11, to the shortened Eu–N bonds after the incorporation of nitrogen.

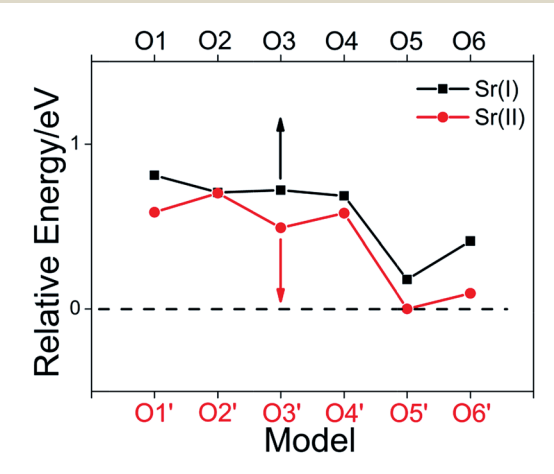


Fig. 14 Relative energy of NSSO models, Sr(i) and Sr(ii) indicate the Eu site, while O1–6 and O1′-6′ indicate the N sites.

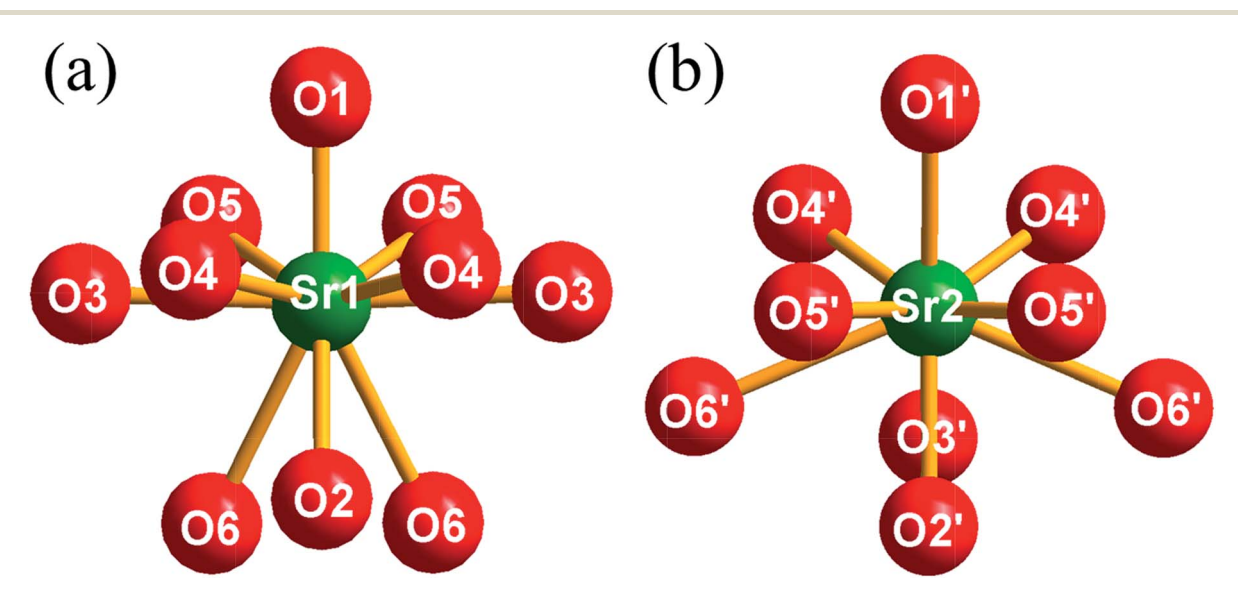


Fig. 13 Local structures of Sr sites in α' -Sr₂SiO₄.

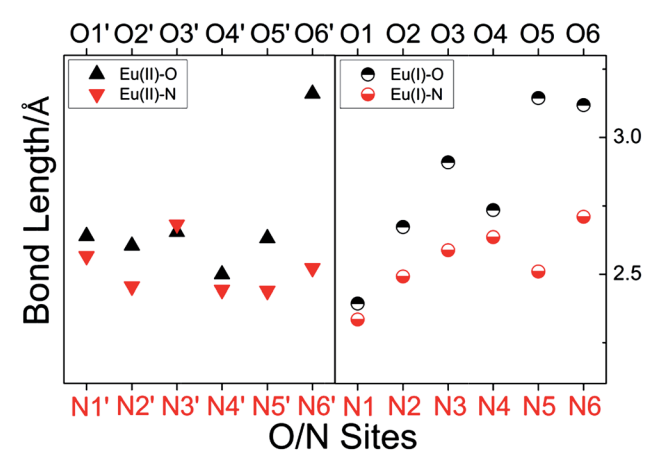


Fig. 15 The bond length variation before and after nitrogen replacing the specific oxygen atom.

To illustrate the red emission of NSSO, we calculate the band structures of SSO and NSSO, as shown in Fig. 16. For clarity, the Fermi level is set to zero. It lies right at the top of the Eu 4f manifold (*i.e.*, valence bands). These bands are of low band energy dispersion in E(k), indicating the large joint density of states, and thus large optical absorption and luminescence. Because PL properties are mainly determined from the top of the valence band (VB) and the bottom of the conduction band (CB), the density of states (DOS) and atom-resolved partial DOS (PDOS) of SSO and NSSO are shown in Fig. 17 to 18, respectively.

As shown in the DOS and PDOS at the top of the VB in Fig. 17, sharp DOS peaks around the Fermi level in SSO are mainly Eu 4f electrons and a minor portion of O 2p electrons. However, for the NSSO model, the broad states include several components. The lowest states are composed of 2p electrons of nitrogen and oxygen atoms. The other states are hybrid orbitals of the Eu 4f electrons and 2p electrons of nitrogen and oxygen. Thus, the short nitrogen coordination distance of Eu leads to the

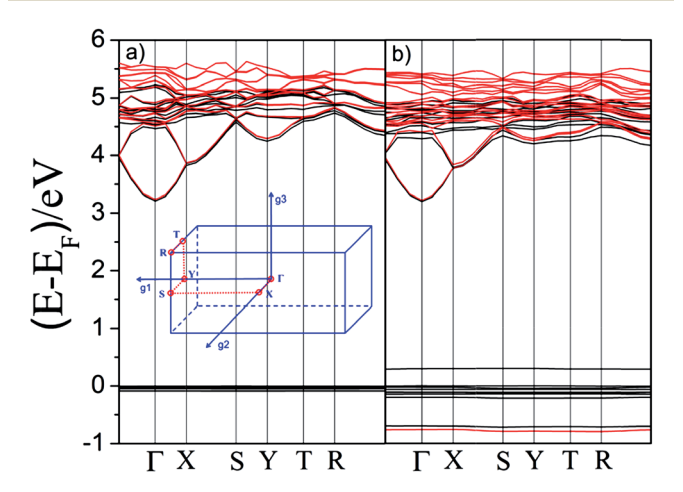


Fig. 16 Band structure of SSO (Eu2, a) and NSSO (Eu2N5', b) models, the inset indicates the Brillouin zone path for band structure calculation.

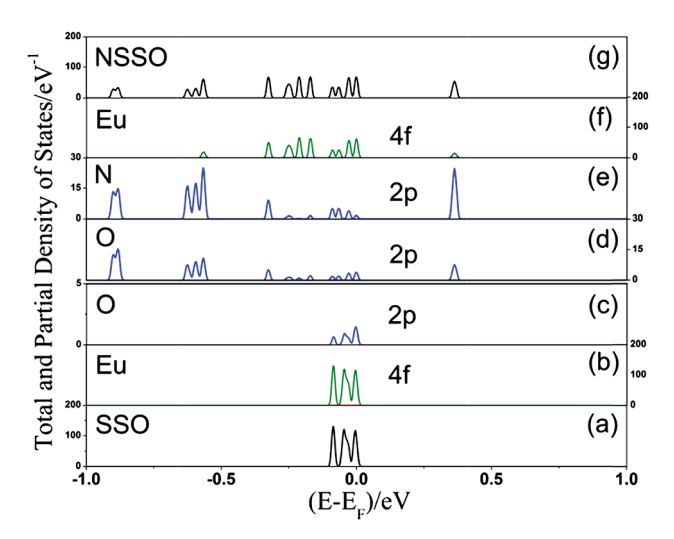


Fig. 17 DOS (a and g) and PDOS (b-f) near the valence band of SSO (a-c) and NSSO (d-g) models, blue line represents p orbitals and green line refers to f orbitals.

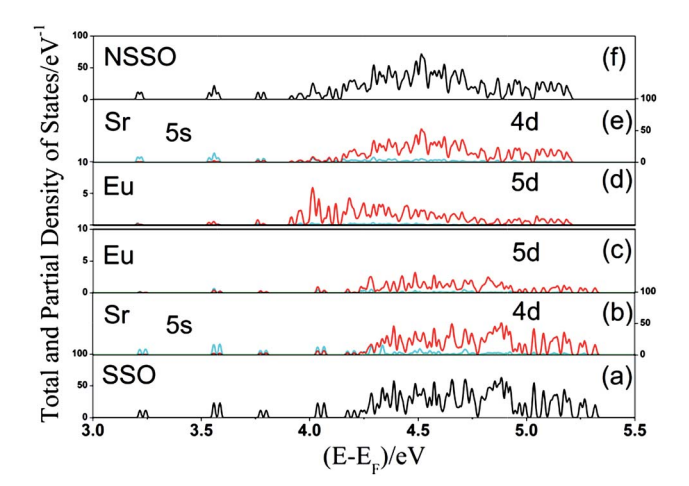


Fig. 18 DOS (a and f) and PDOS (b–e) near the conduction band of SSO (a–c) and NSSO (d–f) models, red line indicates d orbitals and cyan line indicates s orbitals.

hybridization of Eu 4f states and nitrogen/oxygen 2p states, which contributes to the broadened energy states.

As can be seen in Fig. 18, the lower part of the conduction bands is mostly contributed by Sr 5s, Sr 4d and Eu 5d states. Compared with SSO, the Eu 5d states in NSSO models shift to lower energy, and their center of gravity also significantly moves to a lower energy area. This, in combination with the broadened 4f-like states of Eu, leads to the novel red-emission of the PL properties. This variation could also be attributed to the strengthened crystal field effects and nephelauxetic effects caused by the nitrogen coordination of Eu ions.

4 Conclusions

Extra red emission with high thermal stability can be achieved by the incorporation of a small amount of nitrogen into the Sr_2SiO_4 : Eu^{2+} phosphors, which could be attributed to the modification of the local coordination environment of the Eu ions. The modification has been confirmed by both experimental measurements and theoretical simulation. Nitrogen prefers to substitute the O5' site around Eu in $Sr(\pi)$ sites of Sr_2SiO_4 , and the more covalent and shorter Eu-N bonds enable the broadening of Eu 4f energy states and the lower energy shifting of the Eu 5d energy band, leading to the extra redemission.

Acknowledgements

This research was supported by the National Natural Science Foundation of China (no. 51072191, 11179037). We thank Professor Shuyuan Zhang of USTC for helpful discussions and experimental support on HRTEM. We thank Dr Lei Chen of Hefei University of Technology for the fabrication of white LEDs. Moreover, the authors thank BL14W1 beamline of Shanghai Synchrotron Radiation Facility for providing XAFS measurements. Ming-Hsien Lee thanks NCHC for database support and Keywin Electronic Inc. for equipment donation.

Notes and references

- 1 C. He, Y. Guan, L. Yao, W. Cai, X. Li and Z. Yao, *Mater. Res. Bull.*, 2003, **38**, 973.
- 2 C. Guo, D. Huang and Q. Su, *Mater. Sci. Eng.*, *B*, 2006, **130**, 189.
- 3 K. Uheda, N. Hirosaki, Y. Yamamoto, A. Naito, T. Nakajima and H. Yamamoto, *Electrochem. Solid-State Lett.*, 2006, **9**, H22.
- 4 H. Watanabe and N. Kijima, J. Alloys Compd., 2009, 475, 434.
- 5 T. Suehiro, R.-J. Xie and N. Hirosaki, *Ind. Eng. Chem. Res.*, 2014, 53, 2713.
- 6 S. E. Brinkley, N. Pfaff, K. A. Denault, Z. Zhang, H. T. Hintzen, R. Seshadri, S. Nakamura and S. P. DenBaars, Appl. Phys. Lett., 2011, 99, 1106.
- 7 V. D. Luong, W. Zhang and H.-R. Lee, J. Alloys Compd., 2011, 509, 7525.
- 8 H. Nersisyan, H. L. Won and C. W. Won, *Chem. Commun.*, 2011, 47, 11897.
- 9 A. G. Kirakosyan and D. Y. Jeon, *J. Electrochem. Soc.*, 2012, **159**, J29.
- 10 Y. Q. Li, J. E. J. van Steen, J. W. H. van Krevel, G. Botty, A. C. A. Delsing, F. J. DiSalvo, G. de With and H. T. Hintzen, J. Alloys Compd., 2006, 417, 273.
- 11 C. W. Yeh, W. T. Chen, R. S. Liu, S. F. Hu, H. S. Sheu, J. M. Chen and H. T. Hintzen, J. Am. Chem. Soc., 2012, 134, 14108.
- 12 T. Suehiro, R.-J. Xie and N. Hirosaki, *Ind. Eng. Chem. Res.*, 2013, **52**, 7453.
- 13 X. Q. Piao, T. Horikawa, H. Hanzawa and K. Machida, *Appl. Phys. Lett.*, 2006, **88**, 1908.
- 14 T. Suehiro, N. Hirosaki and R. J. Xie, ACS Appl. Mater. Interfaces, 2011, 3, 811.

- 15 J. K. Park, M. A. Lim, C. H. Kim, H. D. Park, J. T. Park and S. Y. Choi, *Appl. Phys. Lett.*, 2003, 82, 683.
- 16 X. Sun, J. Zhang, X. Zhang, S. Lu and X. Wang, J. Lumin., 2007, 122, 955.
- 17 I. Baginskiy, R. S. Liu, C. L. Wang, R. T. Lin and Y. J. Yao, J. Electrochem. Soc., 2011, 158, P118.
- 18 B. G. Hyde, J. R. Sellar and L. Stenberg, *Acta Crystallogr., Sect. B: Struct. Sci.*, 1986, **42**, 423.
- 19 M. Catti, G. Gazzoni and G. Ivaldi, *Acta Crystallogr., Sect. C: Cryst. Struct. Commun.*, 1983, **39**, 29.
- 20 L.-C. Ju, C. Cai, Q.-Q. Zhu, J.-Y. Tang, L.-Y. Hao and X. Xu, *J. Mater. Sci.: Mater. Electron.*, 2013, 24, 4516.
- 21 A. Nag and T. R. N. Kutty, J. Mater. Chem., 2004, 14, 1598.
- 22 K. C. Mishra, M. E. Hannah, A. Piquette, V. Eyert, P. C. Schmidt and K. H. Johnson, ECS J. Solid State Sci. Technol., 2012, 1, R87.
- 23 H. He, R. Fu, X. Zhang, X. Song, X. Zhao and Z. Pan, *J. Mater. Sci.: Mater. Electron.*, 2009, **20**, 433.
- 24 J. Park, S. J. Lee and Y. J. Kim, Cryst. Growth Des., 2013, 13, 5204.
- 25 S. J. Lee, S.-H. Hong and Y. J. Kim, J. Electrochem. Soc., 2012, 159, J163.
- 26 Z. Zhao, Z. Yang, Y. Shi, C. Wang, B. Liu, G. Zhu and Y. Wang, J. Mater. Chem. C, 2013, 1, 1407.
- 27 G. Denis, X. Rocquefelte, P. Deniard, M. H. Whangbo and S. Jobic, *J. Mater. Chem.*, 2009, **19**, 9170.
- 28 W. B. Im, Y.-L. Kim, H. S. Yoo and D. Y. Jeon, *Inorg. Chem.*, 2009, **48**, 557.
- 29 Y.-F. Wang, Q.-Q. Zhu, L.-Y. Hao, X. Xu, R.-J. Xie, S. Agathopoulos and A. Srivastava, *J. Am. Ceram. Soc.*, 2013, 96, 2562.
- 30 J.-Y. Tang, J.-K. Gao, J.-H. Chen, L.-Y. Hao, X. Xu and M.-H. Lee, *Comput. Mater. Sci.*, 2013, 79, 478.
- 31 J. H. Lee and Y. J. Kim, Mater. Sci. Eng., B, 2008, 146, 99.
- 32 X. Piao, K. Machida, T. Horikawa and B. Yun, *J. Lumin.*, 2010, **130**, 8.
- 33 H. S. Jang, Y. H. Won and D. Y. Jeon, *Appl. Phys. B Laser. Optic.*, 2009, **95**, 715.
- 34 J. K. Park, C. H. Kim, S. H. Park, H. D. Park and S. Y. Choi, *Appl. Phys. Lett.*, 2004, **84**, 1647.
- 35 Y. P. Varshni, Physica, 1967, 34, 149.
- 36 M. Catti, G. Gazzoni, G. Ivaldi and G. Zanini, *Acta Crystallogr.*, Sect. B: Struct. Sci., 1983, 39, 674.
- 37 R.-J. Xie, N. Hirosaki, T. Suehiro, F.-F. Xu and M. Mitomo, *Chem. Mater.*, 2006, **18**, 5578.
- 38 H. Liu, Y. Hao, H. Wang, J. Zhao, P. Huang and B. Xu, *J. Lumin.*, 2011, **131**, 2422.
- 39 J. Weil and J. Bolton, *Electron Paramagnetic Resonance: Elementary Theory and Practical Applications*, John Wiley & Sons, Inc., New York, 2007.
- 40 J. Tang, J. Chen, L. Hao, X. Xu, W. Xie and Q. Li, *J. Lumin.*, 2011, **131**, 1101.
- 41 J. G. Sole, L. E. Bausa and D. Jaque, *An Introduction to the Optical Spectroscopy of Inorganic Solids*, John Wiley & Sons, Ltd., England, 2005.